Progress In Electromagnetics Research B, Vol. 67, 71–90, 2016

Topology Measurement of Substation's Grounding Grid by Using Electromagnetic and Derivative Method

Aamir Qamar*, Yang Fan, He Wei, Ammad Jadoon, Muhammad Zeeshan Khan, and Xu Naidong

Abstract—The topology of grounding grid is important for diagnosing its status, which plays a critical role in the safety of personnel and stable operation of power system. The electromagnetic field method and derivative of surface magnetic flux density on the line has been used to measure the branch position in case the grid is parallel to the plane of earth surface that in practice is unknown while the node points and connections were not discussed. This paper introduces a method that uses derivative of surface flux density on circles and lines in a systematic order to find the position of the grid in the plane of the earth surface and connecting the nodes to measure the full topology. This method even identifies any angled branch present in the mesh of a grid. Software simulations and experimental tests verify that the method is feasible and can be applied to identify the topology of a grounding grid.

1. INTRODUCTION

Lightening and short-circuit currents cause surges in the substation that endanger the operation of power system and the lives of personnel working in the substation. The system that ensures the safety of power system and operators working in a substation is known as the Grounding System and the component of the grounding system that provides a low resistance path to the surge currents to flow into the earth and controls the surface potential gradients is called the grounding grid [1–4]. The grounding grid is a network of conductors of certain topology depending on the need, usually rectangular in shape that is made of steel or galvanized steel or even made of copper in some developed countries [5]. As the name indicates, grounding grid is buried inside earth with depth ranges from 0.7 to 1 m and can only be accessed through vertical conductors from the earth surface. The mesh size of a practical grounding grid varies from 3 to 7 m [4].

Since the grounding grid is made of metal or metal alloys and buried in soil, it is almost impossible to know the status of the grid at any time due to corrosion where metals are oxidized making the grid resistive to the flow of fault currents, inefficient and dangerous for the electrical equipment and workers inside a substation [5, 6]. Researchers have been working to find a method that can identify the status of the grid. This includes using the electromagnetic induction method [6, 7], but the method is not applicable in case the grid is corroded, but not broken. Another method previously employed is using Transient Electromagnetic Imaging (TEM) to measure the electrical resistivity of the grounding conductors and locating the breakpoints [8], but the method cannot differentiate between a break point and absence of conductor. Furthermore, the work in [8] did not discuss the corroded branches either. Lastly, some studies have used the Method of moment (MoM) to develop a mathematical formula for the diagnosis, but failed to show the standard value of difference between real and theoretical leakage currents to be considered for the broken conductor [9].

Received 7 March 2016, Accepted 18 April 2016, Scheduled 3 May 2016
* Corresponding author: Aamir Qamar (engr.aamirqamar@yahoo.com).
The authors are with the School of Electrical Engineering, Chongqing University, Campus A, Shapingba, Chongqing 400044, China.

Topology of the grounding grid plays an important role in its status diagnosis because it is difficult to diagnose corroded grid until its topology is known. In some cases due to human error the drawing of the grid is either lost or so much spoiled that it becomes hard to identify the topology. Since excavation is costly and time-consuming methods are to be developed to identify the topology of the grid.

Geophysical prospecting methods are used to determine the location, depth and other fundamental characteristics of underground geological structures and ore bodies. For example, the work in [10] used electrical resistivity tomography and seismic refraction tomography to detect buried cavities, [11] used gravity and magnetic techniques to detect iron ore deposits, [12] used electromagnetic and gamma radiometric data to detect the depth of water table and [13] used electromagnetic technique to detect water table depth and moisture content in soil. Since geophysical prospecting methods are used for large and deeply buried targets, they cannot be used to detect the topology of grounding grid.

In [14], derivative method is used to measure the position of branches of grounding grid. 1st, 3rd and 5th order derivatives of the surface magnetic flux density are taken and the position of the peak shows the position of the branch. But this method is only applicable when the grid is parallel to the plane of earth surface that in practice is not known. In addition, the paper only discusses the branch position, and does not show any method of how to connect the branches and determine the complete topology of the grid. Similarly [15] used 2nd and 4th order derivative to determine the branch position, but was unable to connect the branches. This paper proposes a method to determine the location of the grid in the plane of earth surface by taking the derivative of surface flux density on circle and then using the line and circle derivatives to determine the topology of the grid. The rest of the paper is organized such that Section 2 briefly explains differentiation and derivative of magnetic flux density on line and circle, Section 3 explains the methodology in detail followed by simulation analysis and experimental tests in Sections 4 and 5. Lastly, the conclusion is provided in Section 6.

2. DIFFERENTIATION

Derivatives of data are needed in many scientific applications such as the time derivative d/dt to calculate the speed or velocity or the spatial derivatives, used by [14] and [15] to measure the branch position of the grounding grid. Similarly in [16] and [17] derivative of the seismic data is taken to improve its resolution ratio.

Since derivative is the rate of change of a dependent variable with respect to an independent variable, derivative of a function $f(x)$ is expressed using the finite difference quotient as:

$$\frac{df(x)}{dx} \approx \frac{f(x+h) - f(x)}{h} \tag{1}$$

where h represents the difference between two data point and $f(x+h)$ is the value of function $f(x)$ at adjacent point $x+h$ [18]. In this paper, spatial derivative of magnetic flux density is taken on lines and circles to measure the topology of a grounding grid.

2.1. Line and Circle Derivatives

The concept of line derivative of surface magnetic flux density to measure the position of the branch of the grid has already been presented in [14] and [15]. It is briefly explained here along with the derivative of flux density on circle that leads to the measurement of position or location of a grounding grid in the plane of earth surface and connections verification.

Figure 1 shows a conductor of finite length l lying along y-axis such that its starting point is $(0, 0)$. Let h be the burial depth from the earth surface and I be the current flowing in the conductor. Then, according to Biot-Savart's law the magnetic flux density at point $P(x, y, z)$ is expressed as the following:

$$\vec{B} = \frac{\mu}{4\pi} \int_0^l \frac{I\vec{dl} \times (\vec{r} - \vec{r_d})}{|\vec{r} - \vec{r_d}|^3} \tag{2}$$

where $\vec{dl}$ represents the infinitesimal length element showing the direction of current flow, $\vec{r}$ and $\vec{r_d}$ are the position vectors of point P and $\vec{dl}$ while μ is the magnetic permeability of the medium. In case

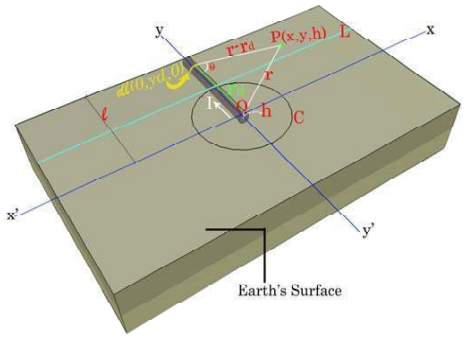

Figure 1. Figure 1 depicts current carrying conductor of length l, buried at depth h, and I is the current flowing in the conductor. Point $P(x, y, z)$ represents the point on earth surface while C and L are the circle and line used to measure the position of the conductor by taking derivative of $\vec{B_z}$ on them.

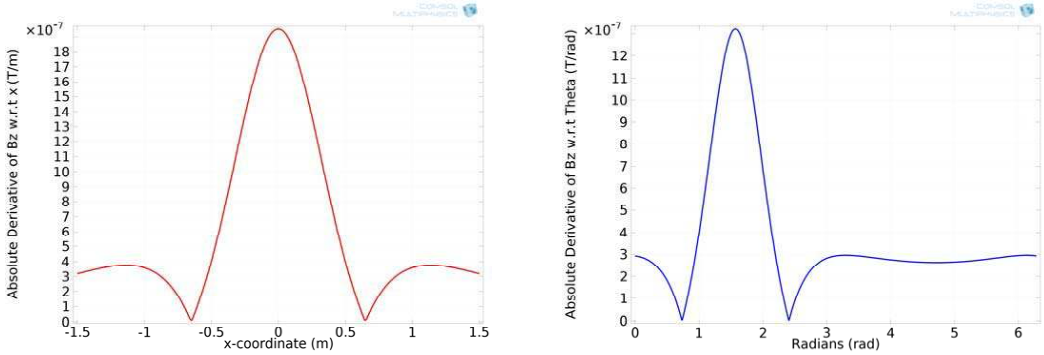

(a) (b)

Figure 2. Figure 2 depicts derivative result of $\vec{B_z}$ on line L and circle C. According to line L the conductor is positioned at $x = 0$ and on circle C it is positioned at '90° (1.57 rad)' that is affirmed by peak positions in 2(a) and 2(b). (a) Absolute derivative of $\vec{B_z}$ on line L. Peak of the graph is positioned at $x = 0$ that confirms the location of buried conductor. (b) Absolute derivative of $\vec{B_z}$ on circle C. Graph illustrates peak at 1.57 rad (90°), which confirms the location of buried conductor. The radius of the circle r_C to generate this graph is taken as 0.7 m.

of Fig. 1, $\vec{dl}$ is $\vec{dy_d}$ because current I flows in the positive y direction. Modifying (2) according to the figure, $\vec{B}$ is the following:

$$\vec{B} = \frac{\mu}{4\pi} \int_0^l \frac{I dy_d \hat{j} \times \left(x\hat{i} + (y - y_d)\,\hat{j} + h\hat{k}\right)}{\left(x^2 + (y - y_d)^2 + h^2\right)^{3/2}} \tag{3}$$

In (3), $\vec{B}$ has three components, but one is enough for the work to be done so selecting the z-component that is

$$\vec{B_z} = \frac{\mu}{4\pi} \int_0^l \frac{I\,(-x) \sin\theta dy_d}{\left(x^2 + (y - y_d)^2 + h^2\right)^{3/2}} \tag{4}$$

Analyzing (4) $\vec{B_z}$ right above the conductor over the earth surface that is when x equals zero and since the flux density is inversely proportional to the square of the distance between the conductor and the given point ($\vec{B_z} \propto \frac{1}{|r - r_d|^2}$), the difference between $\vec{B_z}$ at $x = 0$ and the point next to it on either side of the conductor is high compared to the rest of any two adjacent points on the line or circle resulting in peak at conductor's position. Line L on the earth surface is chosen such that it crosses the conductor

perpendicularly because in the xy-plane if the conductor is lying along one of the axis it is positioned with respect to the other axis and the two axis are always perpendicular. Circle C is chosen such that it centres the starting point of the conductor because in Polar Coordinate System "θ" shows the angle of a geometrical object only when it is connected to the reference point known as Pole. To verify, derivative of $\vec{B}_z$ is taken on the line L and the circle C shown in Fig. 2. Giving a closer look to Figs. 2(a) and 2(b), the position of the peak is at '0' on the line while on the circle it is positioned at '90°(1.57 rad)' that is the same for the position of the conductor beneath the line L and circle C in Fig. 1.

3. METHODOLOGY

As shown in Section 2.1 that the derivative of magnetic flux density on the line or circle identify the position of a buried conductor via the position of the peak obtained, derivatives of surface magnetic flux density on lines and circles are to be used in certain order to measure the topology. The series of steps to be followed are discussed below with the condition that the vertical conductor is connected to a node on the grid. This is because the line for the derivative is to be selected such that over the surface, it is right above the conductor, to prevent the disturbance from any diagonal branch in a mesh.

3.1. Derivative on the Circle Centering the Vertical Conductor

Since this paper is dealing with an inverse problem, derivative on the circle centring the vertical conductor is taken to find the location (angle) of the grid with respect to the x-axis of the assumed xy-plane on the earth surface. This is for the sake of line derivative as the line should be perpendicular to the branches. Once the location (angle) of the grid is determined the position of the vertical conductor is considered as origin $(0, 0)$ while the xy-plane on the earth surface is supposed such that the grid is now parallel to the plane.

3.2. Derivative along X-Axis and Y-Axis Crossing the Origin

In this step line derivative is taken along x and y-axis crossing the origin $(0, 0)$ to locate the branches along each line.

3.3. Ordered Pairs

In this step the position of branches obtained along x and y-axis in the previous step are arranged to form ordered pairs (x, y).

3.4. Plotting and Connecting

As discussed earlier, a grounding grid is a network of metal conductors in which the position of a node is specified by an ordered pair (x, y) in a given plane. The ordered pairs obtained in Section 3.3 are plotted and adjacent pairs are connected to obtain the network.

3.5. Line Derivatives to Obtain the Total Number of Nodes

In this step, line derivatives are taken along x and y-axis to obtain the maximum number of branches that the grid has along x and y-axis, thus finally making ordered pairs and connecting them to obtain the topology of the grid.

3.6. Connection Verification

The grid topology obtained in the last step is not complete because it is not sure whether all adjacent nodes in the grid are connected. To verify this, the connection between two adjacent nodes, circle derivatives are taken on each node.

4. NUMERICAL EXAMPLE

All the simulations presented in this paper are performed in COMSOL Multiphysics 4.4 using the AC/DC module. The numerical model considered for simulation analysis is 5 by 5 square grid made up of copper conductors with dimensions equal to 20×20 m as shown in Fig. 3. The grid has the mesh size equal to 5 m and is buried at depth $h = 0.8$ m in monolayer soil while $I = 10$ A DC is injected at node 1 from the vertical conductor A and flown out of node 14 through conductor B (leakage current into soil is assumed equal to zero). The position of the vertical conductor A is taken as an origin of the xy-plane on the surface. Usually the mesh size of a practical grounding grid ranges from 3 to 7 m and the radius of each circle is taken as 2 m. The steps defined in Section 3 are followed to measure the topology.

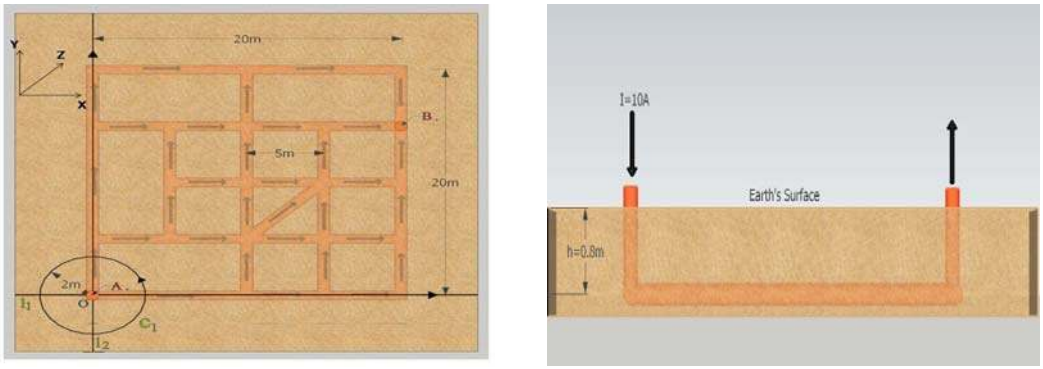

(a) (b)

Figure 3. Simulation model and its features. (a) Top view of the simulation model, lying parallel to plane of earth surface. Dimensions of the grid are 20 m × 20 m and 5 m represents mesh spacing. Distribution of current in the grid is shown by the arrows associated with the grid conductors. Current is injected through vertical conductor A and received through vertical conductor B. c_1 is the circle to determine the location of the grid while l_1 and l_2 show the lines to determine branches position. (b) Side view of the simulation model buried at depth $h = 0.8$ m. DC current $I = 10$ A is injected in the grid.

4.1. Grid Position with Respect to the Plane

Figure 4 shows the derivative of magnetic flux density on c_1. The peaks are positioned at 0° and 90° (1.57 rad) with respect to x-axis, which shows that the grid is lying parallel to the assumed plane.

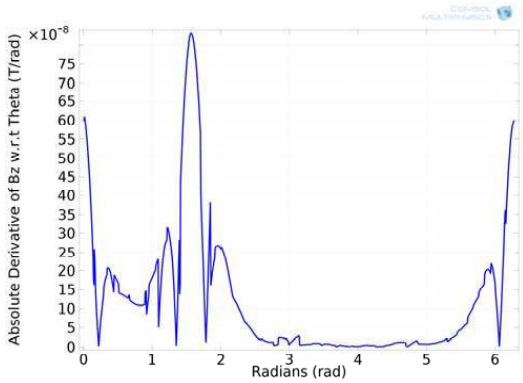

Figure 4. Derivative result of $\vec{B_z}$ on circle c_1. Two peaks are attained at 0 rad (0°) and 1.57 rad (90°) that shows the location of the grid lying at 0° or parallel to the xy-plane.

4.2. Derivative on Lines Crossing the Origin

Taking derivative of $\vec{B_z}$ on l_1 and l_2 gives peaks at points 0, 10, 15, and 20 on x-axis while at points 0, 5, 15, and 20 on y-axis as shown in Fig. 5.

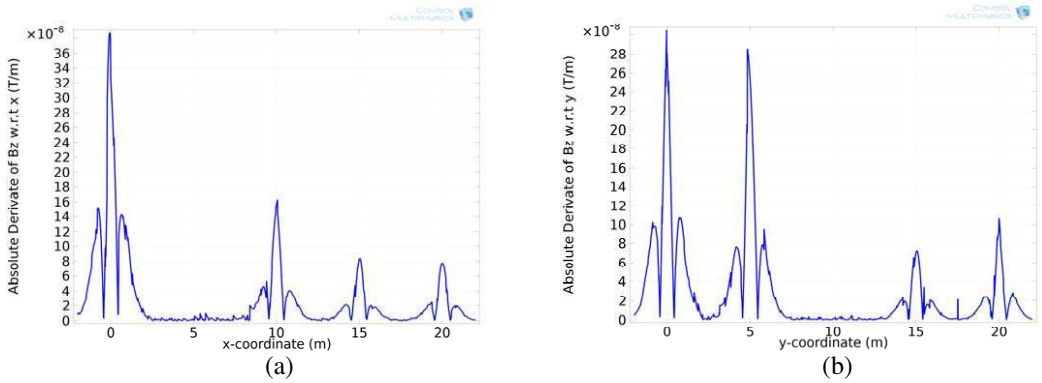

Figure 5. Position of the peaks in 5(a) and 5(b) depicts the position of branches along x and y-axis on line l_1 and l_2. (a) Graph illustrating four peaks at 0, 10, 15 and 20 representing branches location obtained from derivative on line l_1. (b) Graph illustrating four peaks at 0, 5, 15 and 20 representing branches location obtained from derivative on line l_2.

4.3. Ordered Pairs and Connecting

The position of the peaks in Figs. 5(a) and 5(b) are used to make ordered pairs and then connected to form mesh grid.

4.4. Line Derivatives to Obtain the Total Number of Nodes

For convenience, the mesh grid obtained in Fig. 6 is placed on the surface as shown in Fig. 7. Taking the derivative on l_3 results in an additional peak showing the branch along x-axis at position 5. The result of derivative on l_3 is shown in Fig. 8.

Re-pairing, plotting and connecting results in the topology as shown in Fig. 9.

Figure 10 shows the results of derivative on l_4 and l_5 with no additional peaks.

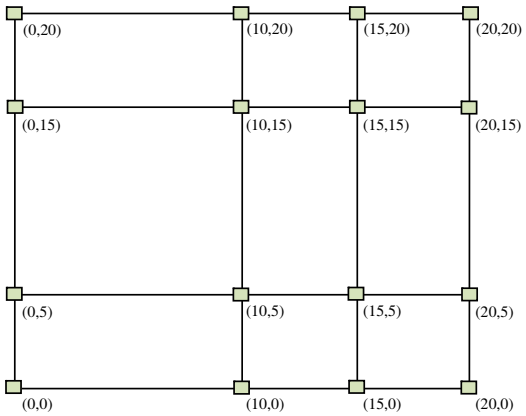

Figure 6. Mesh grid obtained from plotting and connecting the ordered pairs. Position of the peaks in Figs. 5(a) and 5(b) are arranged to form ordered pairs.

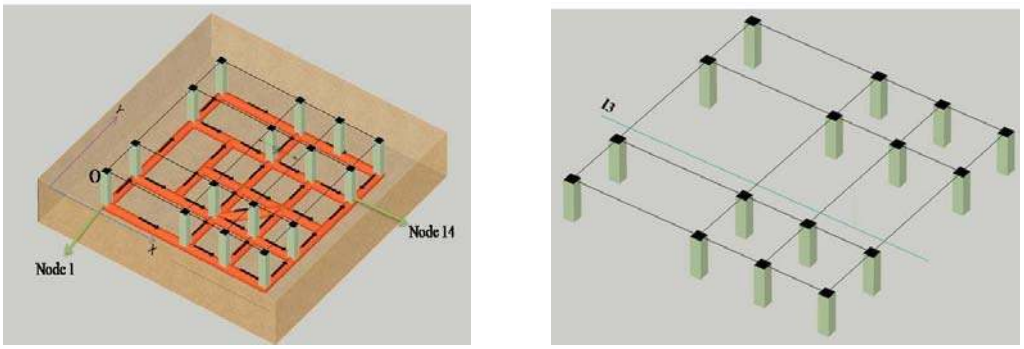

(a) (b)

Figure 7. Figure 7(a) is the mesh grid on the earth surface while 7(b) represents line l_3 along x-axis. (a) Mesh grid in Fig. 6 is illustrated on the earth surface. The node points of the mesh grid are right above the nodes of grounding grid. Current is injected in Node1 and received from Node14. (b) Line l_3 along x-axis right above the conductor on the surface.

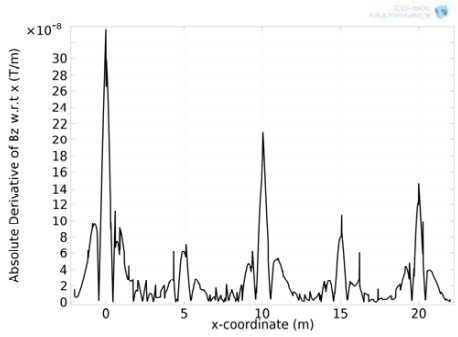

Figure 8. $|B_z'|$ on line l_3 results in five peaks at 0, 5, 10, 15, and 20. Branch is identified from peak at $x = 5$.

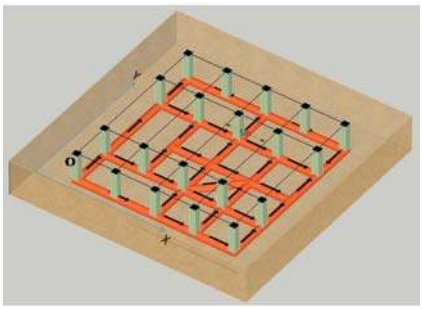

Figure 9. Modified topology due to the presence of branch at $x = 5$.

Figure 11 shows derivative of $\vec{B_z}$ on l_6 that adds additional nodes at $y = 10$ along the x-axis making the topology 5×5 as shown in Fig. 12.

The results of derivative on l_7, l_8, l_9 and l_{10} are shown in Fig. 13, which does not change the topology. The outcome is that the maximum number of branches along x and y-axis are 5 that makes a total of $5 \times 5 = 25$ nodes.

4.5. Connection Verification

The topology obtained in the previous step is a 5×5 topology in, which all the horizontally and vertically adjacent nodes are connected. But it is not known whether all adjacent nodes have a connection. To

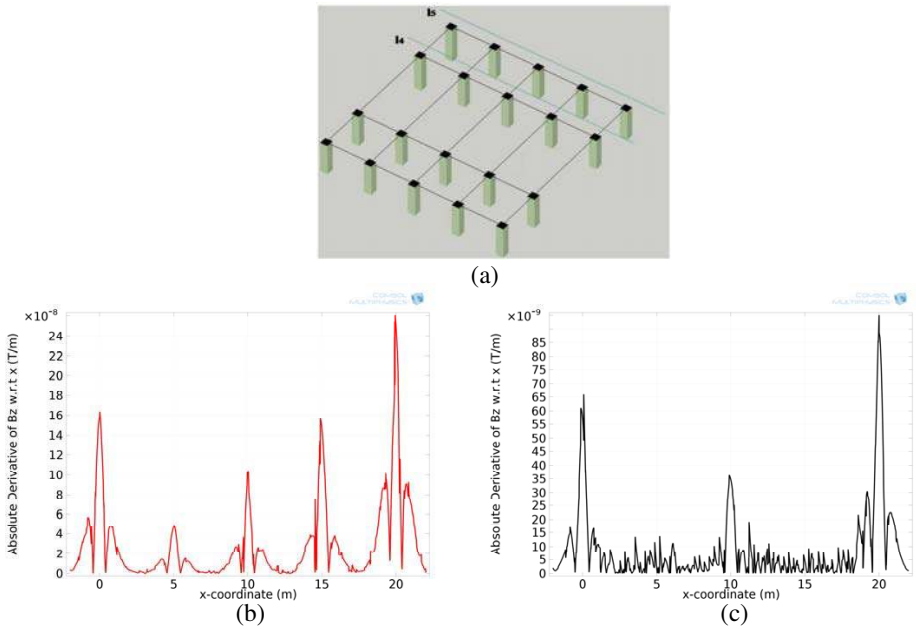

Figure 10. Result illustration of $|B_z'|$ on line l_4 and l_5 along x-axis. (a) Line l_4 and l_5 along x-axis. (b) $|B_z'|$ on line l_4 produces peaks at 0, 5, 10, 15, and 20 along x-axis. (c) $|B_z'|$ on line l_5 produces peaks at 0, 10, and 20 along x-axis.

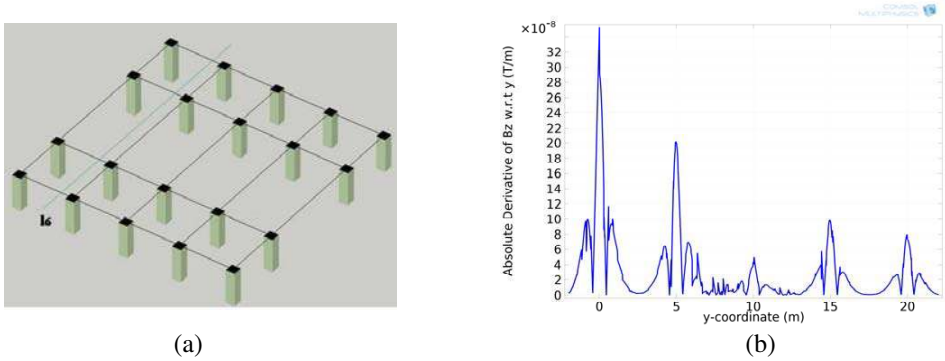

Figure 11. Line l_6 along y-axis and derivative result on it. Peak at $y = 10$ confirms branch at the position. (a) Line l_6 along y-axis. (b) Branches located at 0, 5, 10, 15, and 20 from derivative on line l_6. Peak at $y = 10$ identifies branch at the position.

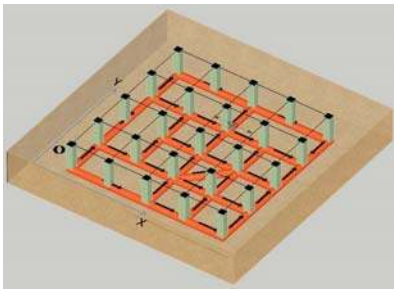

Figure 12. Modified topology due to presence of branch at $y = 10$. Topology is modified by re-arranging the ordered pairs, plotting and connecting them.

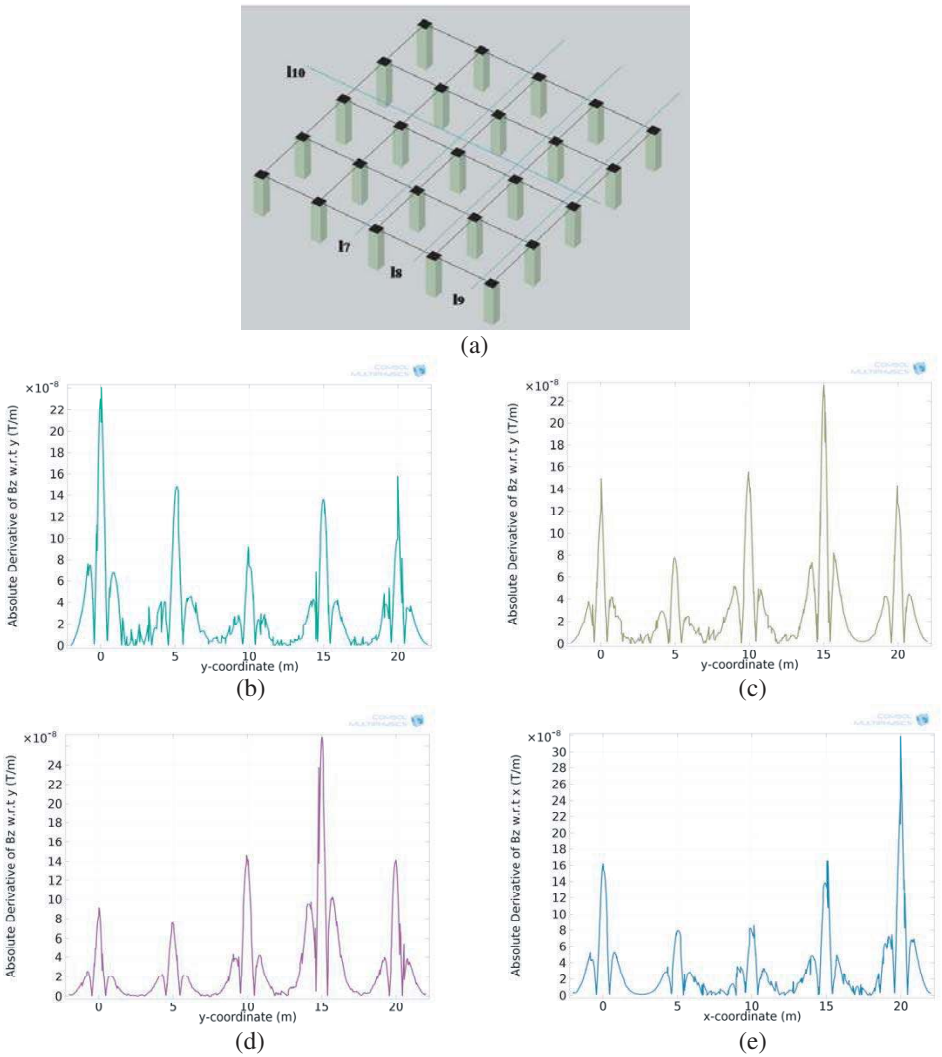

Figure 13. Figure 13(a) shows line l_7, l_8, l_9, and l_{10} while 13(b), 13(c), 13(d), and 13(e) illustrates derivative results. (a) l_7, l_8, and l_9 represent lines along y-axis and l_{10} is line along x-axis. (b) Derivative on line l_7. Peaks at 0, 5, 10, 15, and 20 along y-axis. (c) Derivative on line l_8. Peaks at 0, 5, 10, 15, and 20 along y-axis. (d) Derivative on line l_9. Peaks at 0, 5, 10, 15, and 20 along y-axis. (e) Derivative on line l_{10}. Peaks at 0, 5, 10, 15, and 20 along x-axis. l_{10} is used due to modification in topology after branch is detected at $y = 10$.

verify these connections derivative of $\vec{B_z}$ is taken on circles whose centers are the node points. Fig. 14 shows circles from c_1 to c_{25} while the results of derivative of $\vec{B_z}$ on them are shown in Fig. 15.

To understand the presence and absence of connection between the adjacent nodes in the obtained topology, Figs. 15 and 16 are compared.

Figure 15(a) shows peaks positioned at 0° and 90°(1.57 rad) that confirms connection 1 and 5 while in Fig. 15(b) the peaks are present at 0° and 180°(π rad), which confirms connection 1 and 2, but reject connection 6 showing that node 2 is not a node, but simply a connection. Similarly derivative on c_7 gives peaks at 0°, 90°, 180°, and 270° representing connections 13, 17, 12, and 8. If the results obtained on c_8 and c_{14} shown in 15(h) and 15(n) are examined, peaks are positioned at 0°, 90°, 180°, and 270° confirming connections 12, 16, 11, 7, 22, 26, 21, and 17 while at the same time it is noticed that peak is present at 45°(0.78 rad) in 15(h) and at 225°(3.92 rad) in 15(n), which shows the presence of connection between node 8 and node 14. Removing all the connections not shown by the results in Fig. 15, the final topology is shown in Fig. 17 that is the same as the topology of the grid below the earth surface.

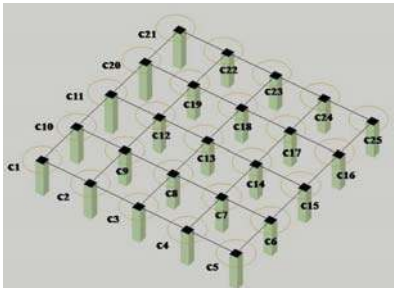

Figure 14. c_1 to c_{25} represent circles to verify connection between two parallel adjacent nodes. Presence of diagonal branch in a mesh is also identified from derivative on circle. Circles center node points to avoid wrong measurement.

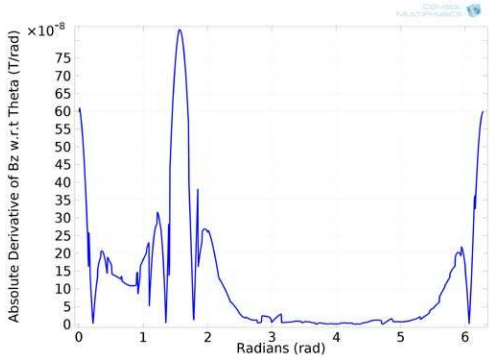

Figure 15a. $|B'_z|$ on circle c_1. Peaks at 0 rad (0°) and 1.57 rad (90°) confirm connection 1 and 5.

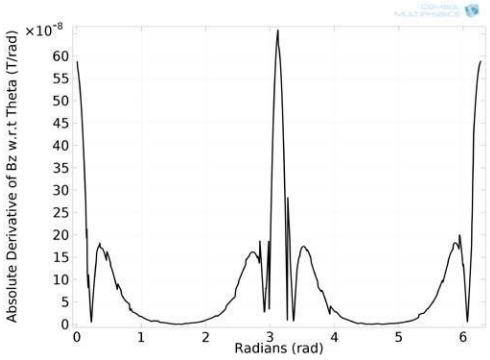

Figure 15b. $|B'_z|$ on circle c_2. Peaks at 0 rad (0°) and 3.14 rad (180°) confirm connection 2 and 1 while no peak at 1.57 rad (90°) for connection 6.

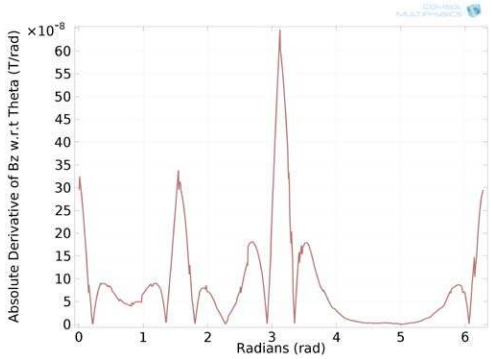

Figure 15c. $|B'_z|$ on circle c_3. Peaks at 0 rad (0°), 1.57 rad (90°), and 3.14 rad (180°) confirm connection 3, 7, and 2.

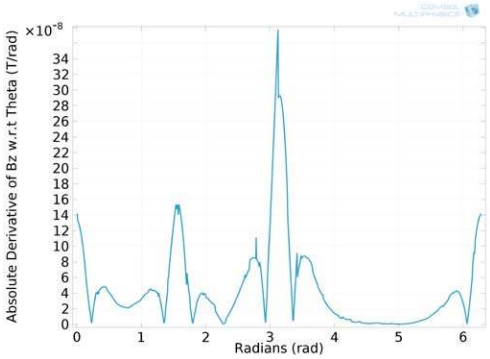

Figure 15d. $|B'_z|$ on circle c_4. Peaks at 0 rad (0°), 1.57 rad (90°), and 3.14 rad (180°) confirm connection 4, 8, and 3.

5. EXPERIMENTAL VERIFICATION

Experimental verification of the method is done by using Hall Effect Probe. The device used to conduct the test features such that its probe is moved by a 3D controller in x, y and z direction with an accuracy of 0.01 mm. The spatial range of the device is from 0 to 400 mm. The measurement values of magnetic flux density are recorded by F. W. BELL 7010 Gauss/Tesla meter, which has an accuracy of 30 mT.

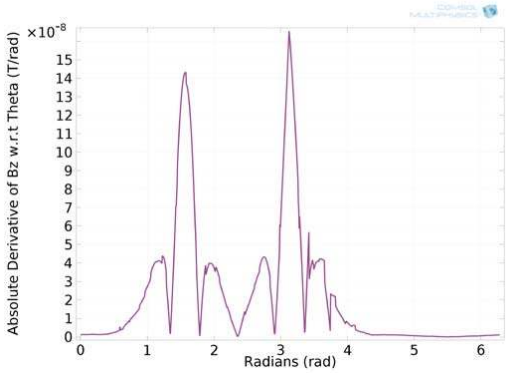

Figure 15e. $|B_z'|$ on circle c_5. Peaks at 1.57 rad (90°), and 3.14 rad (180°) confirm connection 9 and 4.

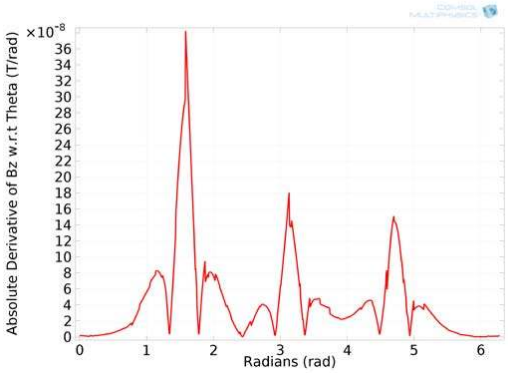

Figure 15f. $|B_z'|$ on circle c_6. Peaks at 1.57 rad (90°), 3.14 rad (180°), and 4.71 rad (270°) confirm connection 18, 13, and 9.

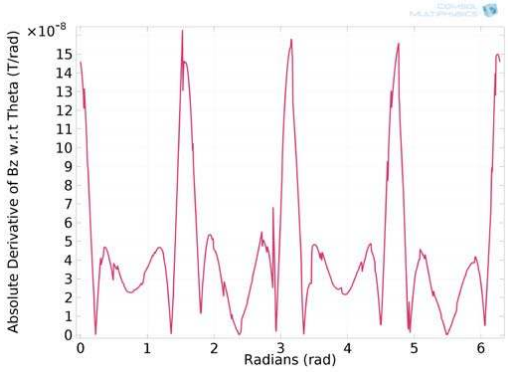

Figure 15g. $|B_z'|$ on circle c_7. Peaks at 0 rad (0°), 1.57 rad (90°), 3.14 rad (180°), and 4.71 rad (270°) confirm connection 13, 17, 12, and 8.

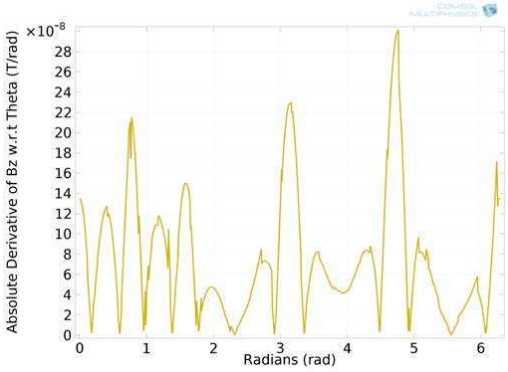

Figure 15h. $|B_z'|$ on circle c_8. Peaks at 0 rad (0°), 1.57 rad (90°), 3.14 rad (180°), and 4.71 rad (270°) confirm connection 12, 16, 11, and 7 while at the same time presence of peak at 0.78 rad (45°) shows diagonal branch.

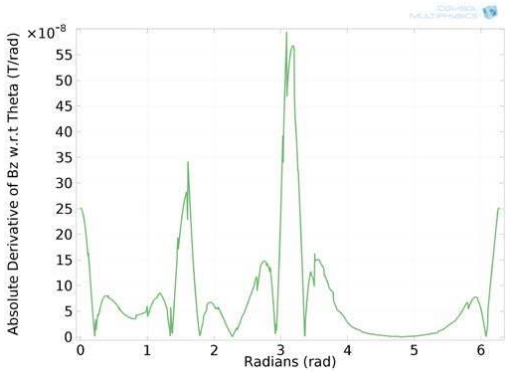

Figure 15i. $|B_z'|$ on circle c_9. Peaks at 0 rad (0°), 1.57 rad (90°) and 3.14 rad (180°) confirm connection 11, 15, and 10 while no peak at 4.71 rad (270°) for connection 6.

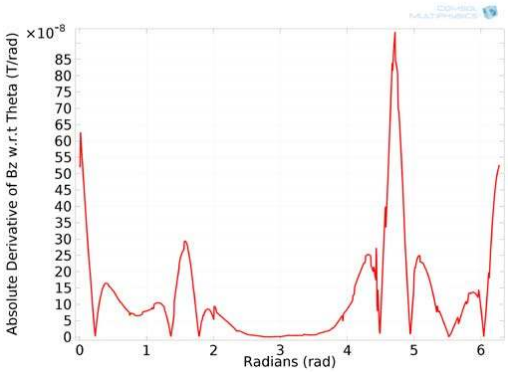

Figure 15j. $|B_z'|$ on circle c_{10}. Peaks at 0 rad (0°), 1.57 rad (90°) and 4.71 rad (270°) confirm connection 10, 14, and 5.

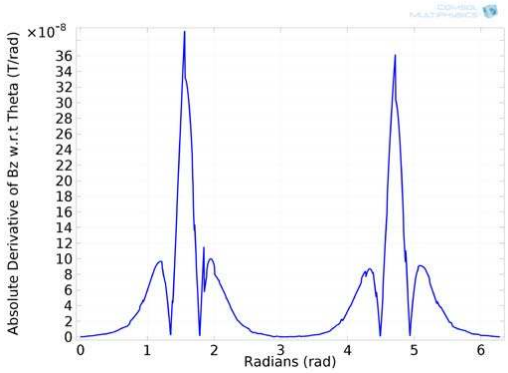

Figure 15k. $|B_z'|$ on circle c_{11}. Peaks at 1.57 rad (90°) and 4.71 rad (270°) confirm connection 23 and 14 while no peak at 0 rad (0°) for connection 19.

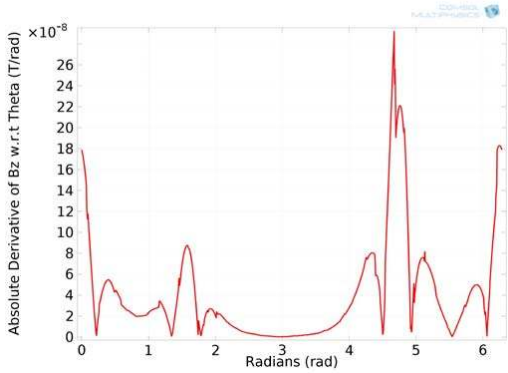

Figure 15l. $|B_z'|$ on circle c_{12}. Peaks at 0 rad (0°), 1.57 rad (90°) and 4.71 rad (270°) confirm connection 20, 24, and 15 while no peak at 3.14 rad (180°) for connection 19.

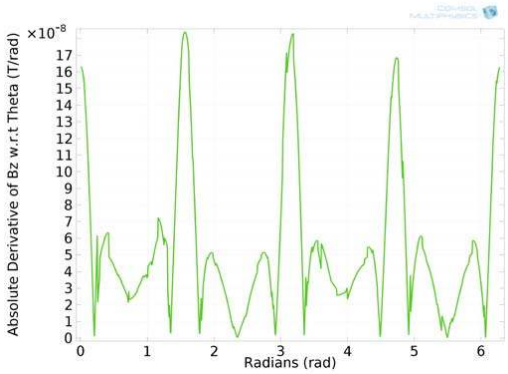

Figure 15m. $|B_z'|$ on circle c_{13}. Peaks at 0 rad (0°), 1.57 rad (90°), 3.14 rad (180°), and 4.71 rad (270°) confirm connection 21, 25, 20, and 16.

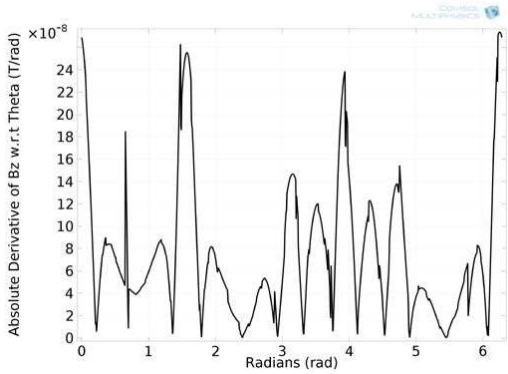

Figure 15n. $|B_z'|$ on circle c_{14}. Peaks at 0 rad (0°), 1.57 rad (90°), 3.14 rad (180°), and 4.71 rad (270°) confirm connection 22, 26, 21, and 17 while at the same time presence of peak at 3.92 rad (225°) shows diagonal branch between node 8 and 14.

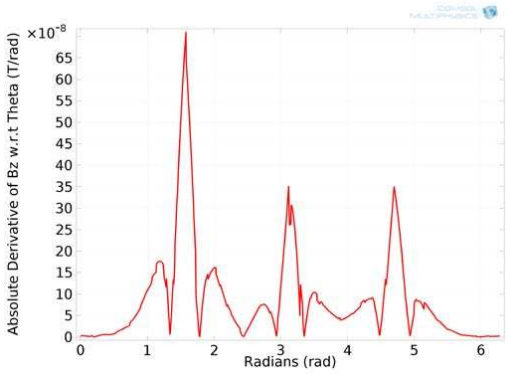

Figure 15o. $|B_z'|$ on circle c_{15}. Peaks at 1.57 rad (90°), 3.14 rad (180°), and 4.71 rad (270°) confirm connection 27, 22, and 18.

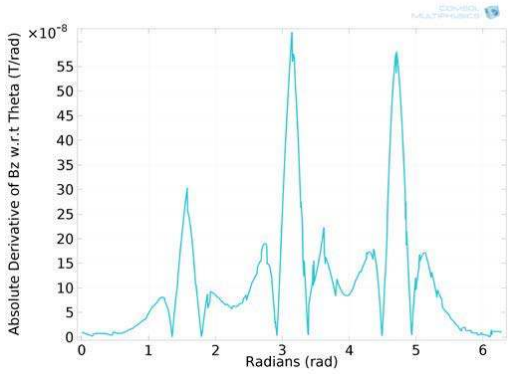

Figure 15p. $|B_z'|$ on circle c_{16}. Peaks at 1.57 rad (90°), 3.14 rad (180°), and 4.71 rad (270°) confirm connection 36, 31, and 27.

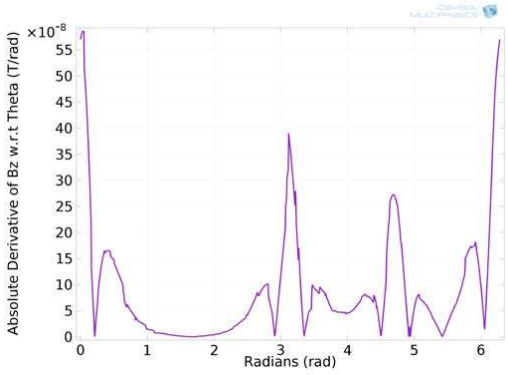

Figure 15q. $|B_z'|$ on circle c_{17}. Peaks at 0 rad (0°), 3.14 rad (180°) and 4.71 rad (270°) confirm connection 31, 30, and 26 while no peak at 1.57 rad (90°) for connection 35.

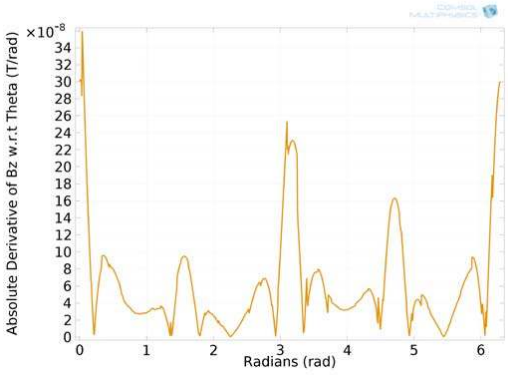

Figure 15r. $|B_z'|$ on circle c_{18}. Peaks at 0 rad (0°), 1.57 rad (90°), 3.14 rad (180°), and 4.71 rad (270°) confirm connection 30, 34, 29, and 25.

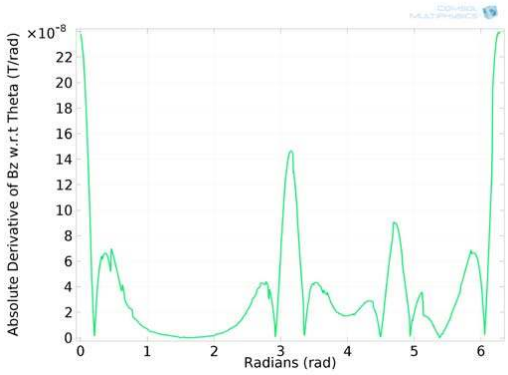

Figure 15s. $|B_z'|$ on circle c_{19}. Peaks at 0 rad (0°), 3.14 rad (180°) and 4.71 rad (270°) confirm connection 29, 28, and 24 while no peak at 1.57 rad (90°) for connection 33.

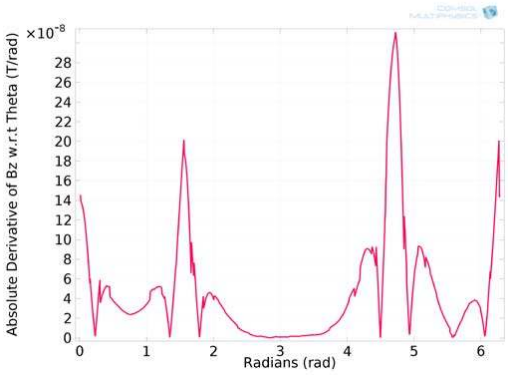

Figure 15t. $|B_z'|$ on circle c_{20}. Peaks at 0 rad (0°), 1.57 rad (90°) and 4.71 rad (270°) confirm connection 28, 32, and 23.

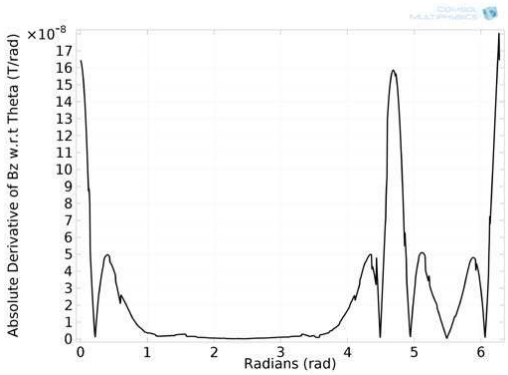

Figure 15u. $|B_z'|$ on circle c_{21}. Peaks at 0 rad (0°) and 4.71 rad (270°) confirm connection 37 and 32.

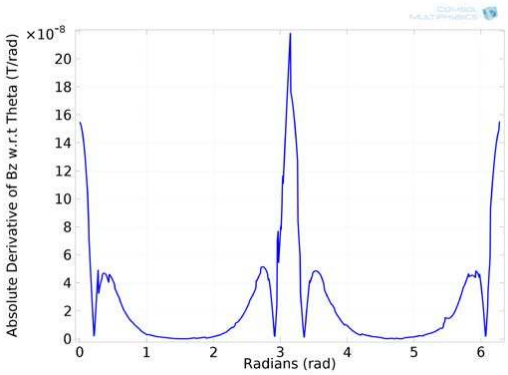

Figure 15v. $|B_z'|$ on circle c_{22}. Peaks at 0 rad (0°) and 3.14 rad (180°) confirm connection 38 and 37 while no peak at 4.71 rad (270°) for connection 33.

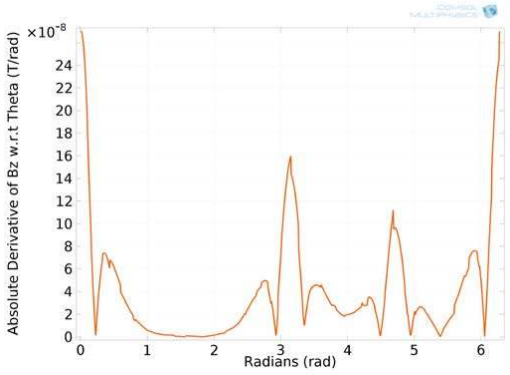

Figure 15w. $|B_z'|$ on circle c_{23}. Peaks at 0 rad (0°), 3.14 rad (180°) and 4.71 rad (270°) confirm connection 39, 38, and 34.

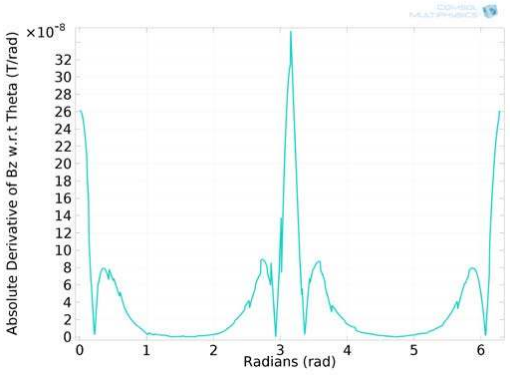

Figure 15x. $|B_z'|$ on circle c_{24}. Peaks at 0 rad (0°) and 3.14 rad (180°) confirm connection 40 and 39 while no peak at 4.71 rad (270°) for connection 35.

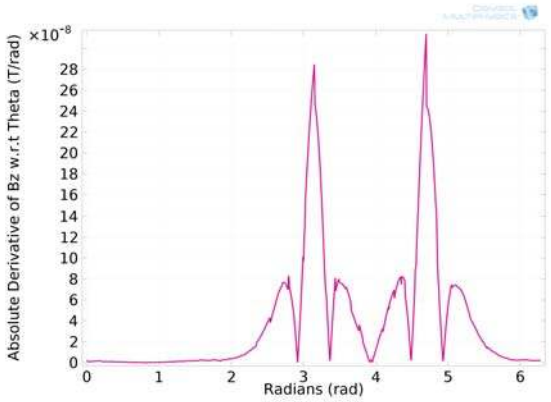

Figure 15y. $|B_z'|$ on circle c_{25}. Peaks at 3.14 rad (180°) and 4.71 rad (270°) confirm connection 40 and 36.

Figure 15. Illustration of derivative results on circle c_1 to c_{25}.

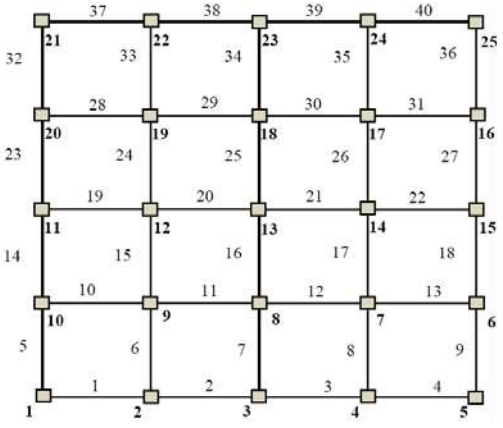

Figure 16. Obtained topology. Branches are numbered from 1 to 40 and 1 to 25 bold text represent nodes.

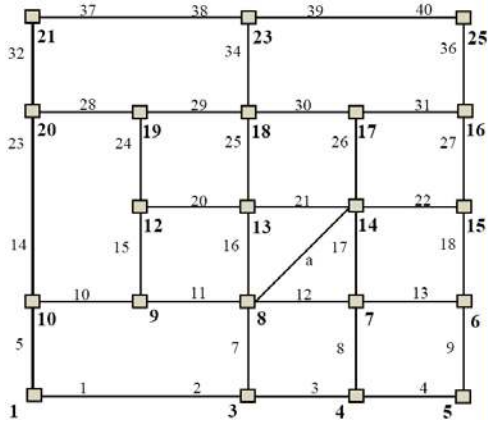

Figure 17. Final topology measured. 'a' is the diagonal branch identified between node 8 and 14. This figure is drawn by removing unconfirmed connections in Fig. 16.

(a) (b)

Figure 18. Experimental model and lab test. (a) Illustration of 5×5 square grid made of copper wires. The dimensions of the grid are 360 mm $\times$ 360 mm and mesh spacing is 90 mm. DC current is injected at Node1 and received from Node14. (b) Lab test.

Initially the position of the device with respect to the table is adjusted and the probe is positioned (0, 0, 0).

The grid used to perform the experiment is 5×5 square grid made of copper wires. The dimensions of the grid are equal to 360×360 mm that equates mesh size equal to 90 mm. DC current of $I = 9.22$ A is injected into the grid at node 1 from the vertical conductor (vertically downward to avoid the influence of current source lead) and received from node 14. As the current flows flux density is measured at $h = 10$ mm above the grid. Fig. 18 shows the model and device used to perform the experiment.

Figure 19 depicts the circles c_1, c_{11}, c_{13} and lines from l_1 to l_{10} (direction of the arrow represents the direction of measurement taken) while Fig. 20 shows the results obtained. The subscript for l and c indicates the count as well as the sequence. 127 equally spaced (3 mm) points are taken on each line while the number of points taken on each circle are 100 that are equally spaced at distance of 3.768 mm. The radius of each circle is chosen $r = 60$ mm and since the device can only move along the line, points on circle are set using trigonometric equations $x = r\cos\theta$ and $y = r\sin\theta$. Due to EMI in the surroundings and noise caused by differentiation, the original data fluctuates along the axis. Moving Average Technique also known as Moving or Rolling Mean has been used to smooth the original data, which is a statistical technique in, which a sliding window of a certain length is used to find the average and assigned to the location of window. In this work, a window length of three data points was used where each filtered data point was the average of the previous, present and the next data point. This technique is effectively a low-pass filtering using a finite impulse response filter.

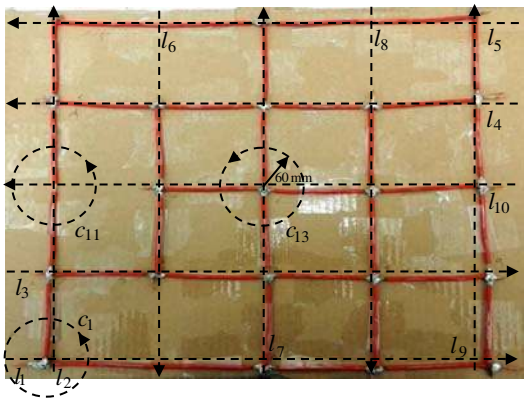

Figure 19. Illustration of circles and lines to measure the topology of the model. Direction of arrows represent direction of measurement taken. Subscript for c and l represents number and sequence.

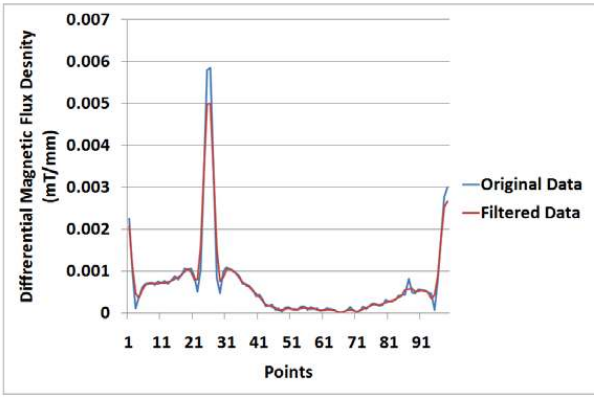

Figure 20a. $|B'_z|$ on circle c_1. Peaks attained at point 1 (0°) and 25 (90°) shows the grid is parallel to the assumed plane. Connection 1 and 5 in Fig. 22 is also verified.

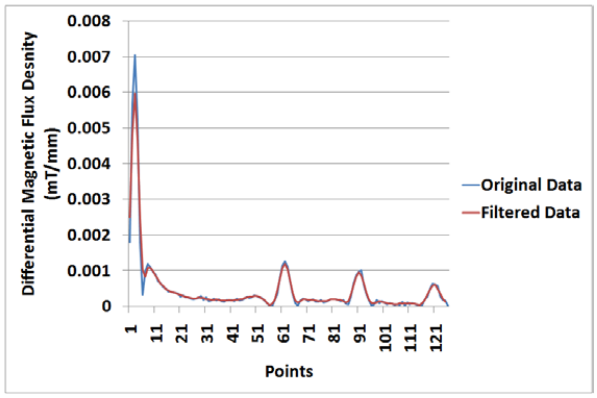

Figure 20b. Graph illustrating four peaks at point 4, 64, 94, and 124 representing branches location obtained from derivative on line l_1.

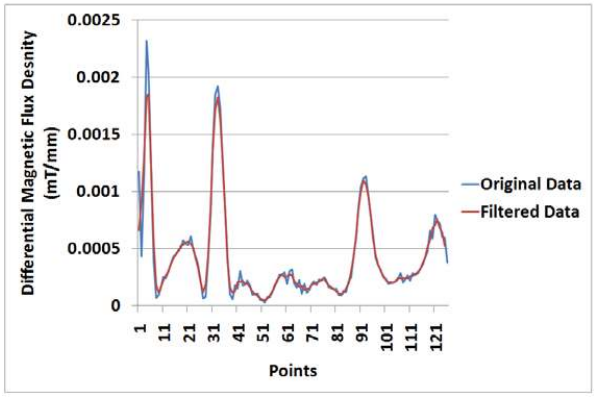

Figure 20c. $|B'_z|$ on line l_2. Peaks at point 4, 34, 94, and 124.

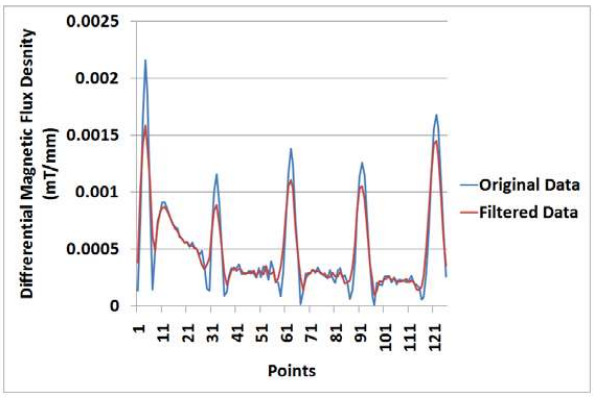

Figure 20d. Branches located at 4, 34, 64, 94, and 124 from derivative on line l_3. Peak at point 34 identifies branch at the position.

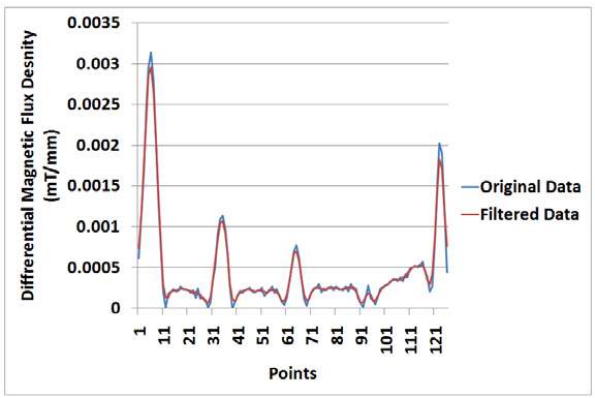

Figure 20e. $|B'_z|$ on line l_4. Peaks at point 4, 34, 64, 94, and 124.

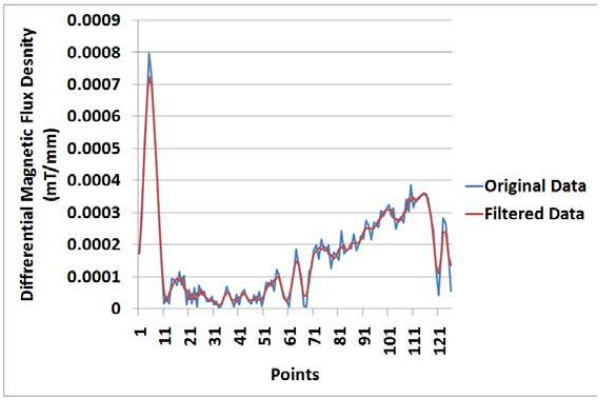

Figure 20f. $|B'_z|$ on line l_5 produces peak at point 4, 64, and 124.

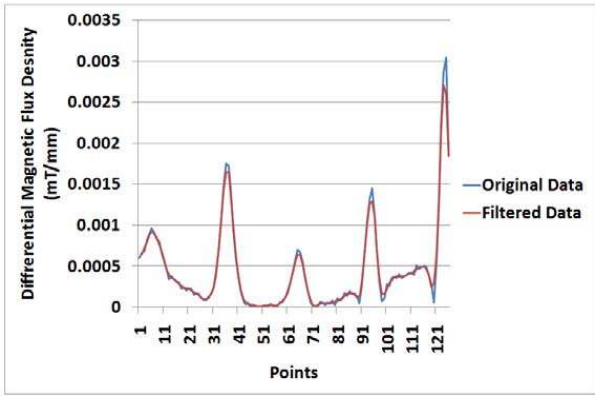

Figure 20g. $|B'_z|$ on line l_6 results in five peaks at 4, 34, 64, 94, and 124. Branch is identified from peak at point 64.

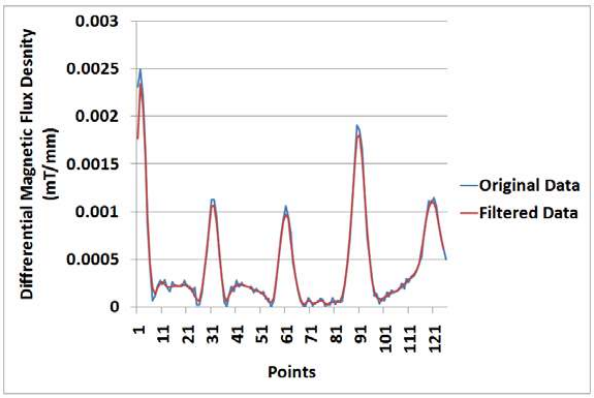

Figure 20h. $|B'_z|$ on line l_7. Peaks at point 4, 34, 64, 94, and 124.

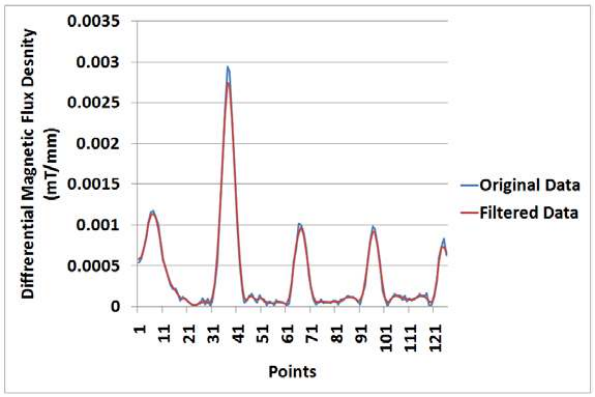

Figure 20i. $|B'_z|$ on line l_8. Peaks at point 4, 34, 64, 94, and 124.

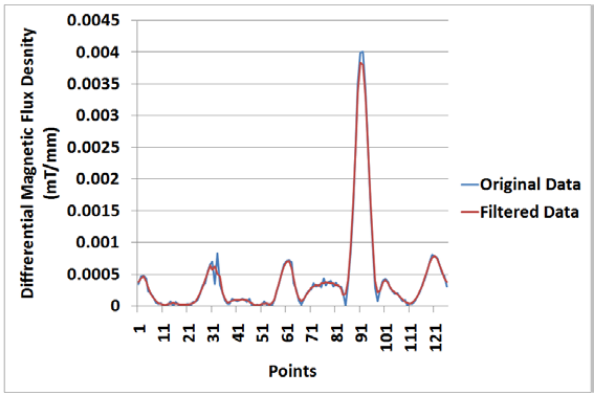

Figure 20j. $|B'_z|$ on line l_9. Peaks at point 4, 34, 64, 94, and 124.

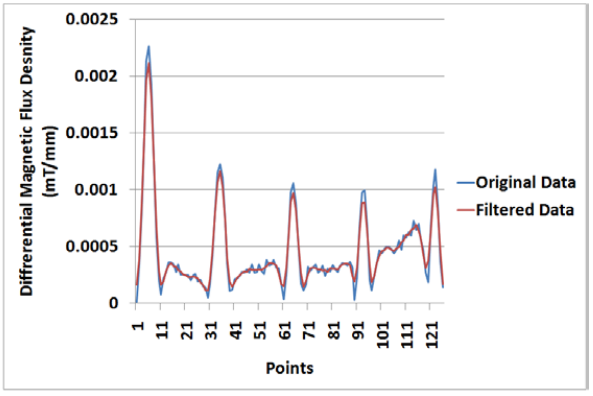

Figure 20k. $|B'_z|$ on line l_{10}. Peaks at point 4, 34, 64, 94, and 124.

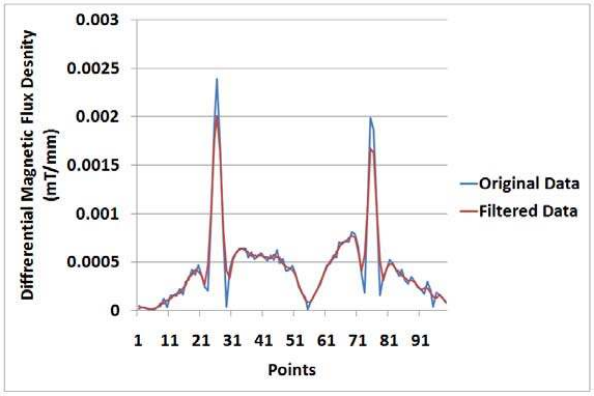

Figure 20l. $|B'_z|$ on circle c_{11}. Peaks at point 25 (90°) and 75 (270°) confirm connection 23 and 14 while absence of peak at point 1 (0°) rejects connection 19.

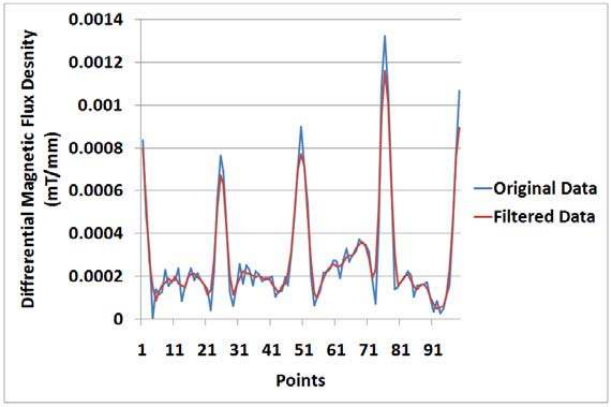

Figure 20m. $|B'_z|$ on circle c_{13}. Peaks at point 1 (0°), 25 (90°), 50 (180°), and 75 (270°) confirm connection 21, 25, 20, and 16.

Figure 20. Figures 20(a), 20(l), and 20(m) depicts result on circle c_1, c_{11} and c_{13} while 20(b) to 20(k) shows result of derivative of magnetic flux density on line l_1 to l_{10}. Blue colour graph represents original while reddish-brown shows filtered data.

The test is conducted following the steps defined in methodology. Firstly, to measure the location (angle) of the grid, derivative of magnetic flux density is taken on c_1 that centres the vertical conductor (origin (0, 0)). Fig. 20(a) shows the result in, which peaks are, positioned at point 1(0°) and 25(90°) confirming that the grid is parallel to the assumed axis. Subsequently, the derivative on lines crossing the origin are taken along x and y-axis that are l_1 and l_2. 20(b) and 20(c) has the result showing peaks at points 4, 64, 94, and 124 along x-axis while at points 4, 34, 94, and 124 along y-axis. One thing to keep under consideration is, that the positions of the peaks in the figures showing the result of derivative on lines and circles may not be so accurate because of the ductility of the copper material and human error while making the grid. Making ordered pairs of the above points and connecting the parallel adjacent ordered pairs as shown in Fig. 21.

Next is to take derivative on l_3 to l_{10} shown in Fig. 20(d) to 20(k). Only derivative on l_3 and l_6 shows additional branch along x and y-axis changing the topology in to 5×5 shown in Fig. 22. Fig. 20(a) confirms connections 1 and 5, derivative on c_{11} gives peaks at point 25 and 75 verifying connections 23 and 14 while connection 19 should be removed. Similarly Fig. 20(m) confirms connections 21, 25, 20 and 16 by showing peaks at point 1, 25, 50 and 75. The final topology is obtained when the connections are confirmed using the results obtain from derivative of flux density on circles centring the node points.

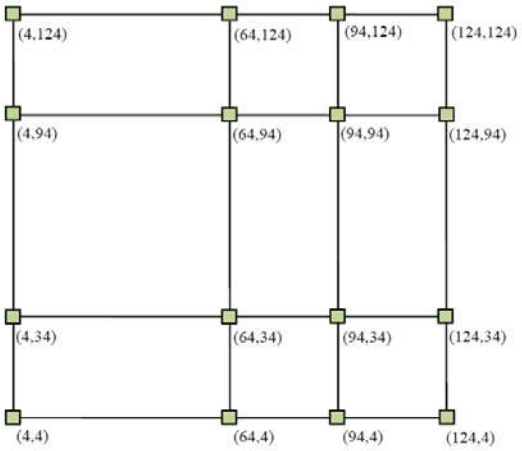

Figure 21. Mesh grid created by connecting the ordered pairs attained from derivative on line l_1 and l_2. Ordered pairs represent node points.

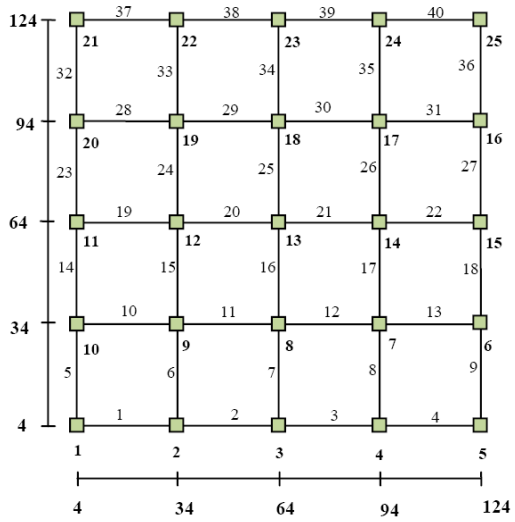

Figure 22. Obtained topology due to line derivatives. 1 to 40 represents number of branches while 1 to 25 represent nodes.

6. CONCLUSION

Based on electromagnetic field and derivative method, [14] and [15] only achieved to measure branch location for grounding grid located parallel to the plane of earth surface. In practice, the location of grounding grid is unknown. This paper presented a method that not only locates grounding grid but at the same time measures its complete topology. This method is also feasible for the topology of the grid containing diagonal branch. Numerical example and lab test show that the method is feasible to solve the problem of unknown grounding grids.

ACKNOWLEDGMENT

This work is supported by the National Natural Science Foundation of China (Grant No. 51477013).

REFERENCES

1. Zhang, X., T.-Z. Yu, and X. Yin, "The corrosion break-point diagnosis method of grounding grid based on the principle of uniting magnetic field and electric circuit," *IEEE*, 2010.
2. Zhang, B., J. Wu, J. He, and R. Zeng, "Analysis of transient performance of grounding system considering soil ionization by time domain method," *IEEE Transaction on Magnetics*, Vol. 49, 1837–1840, May 2013.
3. Hideki, M., "Electromagnetic transient response of buried bare wire and ground grid," *IEEE Transactions on Power Delivery*, Vol. 22, 1673–1679, Jul. 2007.
4. IEEE Guide for Safety in AC Substation Grounding, IEEE Standard 80-2000.
5. Wang, S., J. Liu, J. Wang, Z. Li, and S. Wang, "Conductor corrosion fault detection & identification for grounding grids," *The 3rd International Conference on Innovative Computing Information and Control, IEEE*, 2008.
6. Liu, Y., X. Cui, and Z. Zhao, "Corrosion diagnosis for grounding grids by using electromagnetic induction method," *Automation Congress*, WAC 2008 World, 2008.
7. Dawalibi, F. P., "Electromagnetic fields generated by overhead and buried short conductors. Part 2 — Ground conductor," *IEEE Transactions on Power Delivery*, Vol. 1, 112–119, Oct. 1986.

8. Yu, C., Z. Fu, X. Hou, H.-M. Tai, and X. Su, "Break point diagnosis of grounding grids using transient electromagnetic apparent resistivity imaging," *IEEE Transactions on Power Delivery*, 2015.
9. Zhang, B., Z. Zhao, X. Cui, and L. Li, "Diagnosis of breaks in substation's grounding grid by using the electromagnetic method," *IEEE Transactions on Magnetics*, Vol. 38, No. 2, Mar. 2002.
10. Cardarelli, E., M. Cercato, A. Cerreto, and G. Di Filippo, "Electrical resistivity and seismic refraction tomography to detect buried cavities," *Geophys Prospect*, Vol. 58, 685–695, 2010.
11. Vincent, A., M. Charles, A. Willis, and M. Gerald, "Geophysical exploration of iron ore deposit in Kimachia area in Meru county in Kenya, using gravity and magnetic techniques," *Int. J. Sci. Res. (IJSR)*, Vol. 2, 104–108, 2013.
12. Buchanan, S. and J. Triantafilis, "Mapping water table depth using geophysical and environmental variables," *Ground Water*, Vol. 47, 80–96, 2009.
13. Hedley, C. B., P. Roudier, I. J. Yule, J. Ekanayake, and S. Bradbury, "Soil water status and water table depth modelling using electromagnetic surveys for precision irrigation scheduling," *Geoderma*, Vol. 199, 22–29, 2013.
14. Wang, X., C. Li, W. He, F. Yang, D. Yao, and X. Kou, "Topological measurement and characterization of substation grounding grid based on derivative method," *International Journal of Electrical Power and Energy Systems*, 2014.
15. Wang, X., W. He, F. Yang, L. Zhu, and X. Liu, "Topology detection of grounding grids based on derivative method," *Transactions of China*, Feb. 2015.
16. Yu, H. and X. Ying, "Derivative seismic processing method for GPR data," *IEEE Int. Geosci. Rem. Sens.*, Vol. 1, 145–147, 1997.
17. Liu, Q., "Sensitivity and Hessian matrix analysis of power spectral density functions for uniformly modulated evolutionary random seismic responses," *Finite Elem. Anal. Des.*, Vol. 48, 1370–5, 2012.
18. Philipp, O. and J. Scherer, *Computational Physics, Simulation of Classical and Quantum Systems*, 2nd edition, Springer, 2013.